nature communications

Article

https://doi.org/10.1038/s41467-026-70259-9

Fast-swimming biohybrid OstraBot with self-trained high-strength muscles

Received: 12 September 2025

Accepted: 24 February 2026

Pengyu Chen[1], Xuchen Wang[1], Jinrun Zhou[1] & Yu Jun Tan[1,2] ✉

Limited muscle force generation remains a major bottleneck in developing stronger, faster, and more efficient biohybrid robots. We present a fully autonomous self-training platform that strengthens skeletal muscle tissues by harnessing their robust spontaneous contractions. This approach produced muscle actuators with a maximum force of 7.05 mN and a stress of 8.51 mN/mm^2, the highest reported for C2C12-derived muscle actuators. To demonstrate their capabilities, we developed a twin-tail muscle-powered ostraciiform swimming robot, OstraBot, and guided its design using a physiology-based muscle contraction model. Model-informed analysis identified stiffness–frequency combinations that maximized muscle energy output, enabling a top speed of 467 mm/min (15.6 body lengths/min), significantly outperforming previously reported skeletal muscle-powered biohybrid robots. The robot demonstrated strong thrust generation and precise on–off controllability through sound-triggered clapping control. This work establishes a versatile platform for producing high-strength skeletal muscle actuators and quantitatively guiding the robotic design for high-performance biohybrid robots.

In the search for actuator materials that are sustainable, energy-efficient, and capable of adaptive motion, engineered biological muscle tissues have emerged as a promising alternative to synthetic abiotic materials[1–4]. Skeletal muscle, in particular, provides on-demand contractility[5] and modular scalability[6], which has enabled the development of skeletal muscle-driven robots such as biohybrid walking machines[7–9] and robotic manipulators[10–14]. Despite these demonstrations, progress in biohybrid robot research has been constrained by a common bottleneck: the limited force generation of engineered skeletal muscle tissues. This limitation reduces locomotive speed, payload capacity, and overall versatility, preventing biohybrid systems from achieving the complexity and performance seen in robots powered by conventional actuators.

The need to overcome this challenge has motivated numerous recent studies into enhancing the force output of muscle actuators. One approach is to use primary skeletal muscle cells from murine[13,15] or human[10,12] sources. Although they generate higher intrinsic forces, these cells are less sustainable, show batch-to-batch variability, and are difficult to culture at scale[16,17]. Immortalized myoblast lines, most notably C2C12, remain widely used in biohybrid robots, despite producing weaker active forces than primary cells under conventional maturation conditions. Efforts to enhance the strength of C2C12 muscle tissues have focused on introducing biological cues, such as growth factors[18] or coculture with photosynthetic algae[19], and on active training approaches, including mechanical and electrical stimulation[20–23], which improve myotube alignment and functional maturation. Despite these strategies, most C2C12 muscle tissues generate < 1 mN of active force, with only a few reports exceeding 2 mN, and corresponding stresses consistently remaining below 2 mN/mm^2.

Here, we introduce an arm-wrestling-inspired self-training strategy that enables C2C12 skeletal muscle tissues to generate a maximum force of 7.05 mN (8.51 mN/mm^2), markedly exceeding previously reported values for biohybrid robots. This autonomous, scalable training platform converts spontaneous contractions of early-developing muscle tissues into repeated lengthening–shortening cycles, increasing muscle force without specialized equipment or

---

[1]Department of Mechanical Engineering, College of Design and Engineering, National University of Singapore, Singapore, Singapore. [2]Advanced Robotics Centre (ARC), National University of Singapore, Singapore, Singapore. ✉e-mail: yujun.tan@nus.edu.sg

manual intervention. We also developed a physiology-based predictive model linking muscle mechanics to robotic performance, enabling model-informed design and control to fully exploit muscle contractile potential. Leveraging the strong muscle tissues and the contraction model, we built a biohybrid swimming robot, OstraBot, which achieved a swimming speed of 467 mm/min (15.6 body lengths/min)—the fastest locomotion reported for skeletal muscle-driven biohybrid robots.

Results

Arm-wrestling-inspired self-training mechanism

Just as humans build strength through exercise, engineered muscle tissues can also become stronger when mechanically trained[24,25]. Inspired by the dynamics of an arm-wrestling contest, we developed a self-training platform in which a pair of engineered skeletal muscle tissues is mechanically coupled to generate autonomous, reciprocal training cycles (Fig. 1a). After molding, the muscle rings underwent initial matrix remodeling and compaction in the polydimethylsiloxane (PDMS) molds (Supplementary Fig. 1). A pair of compacted muscle tissues was then transferred to the self-training platform, each with one end anchored to the stationary base and the other connected to the sliding block. As the muscle pair progressively differentiated, the two tissues began actively pulling against each other, generating continuous mechanical loading that strengthened and aligned both tissues over time. C2C12 skeletal muscle actuators produced using our self-training platform exhibited markedly higher force output and powered biohybrid robots with substantially greater locomotion speeds compared to previously reported systems[7–9,15,21,23,26–34] (Fig. 1b, Supplementary Table 1).

The autonomy of the self-training behavior originates from the intrinsic spontaneous contraction of skeletal muscle tissues. We observed that C2C12 skeletal muscle tissues exhibited robust spontaneous contraction at early stages of differentiation, even in the absence of external stimulation (Fig. 1c). The spontaneous contraction behavior emerged 3 days after initiating differentiation, with contraction amplitude further strengthened at day 4 and plateaued by day 5–7. After day 7, the spontaneous contractions gradually diminished and became barely detectable by day 14 (Fig. 1d, Supplementary

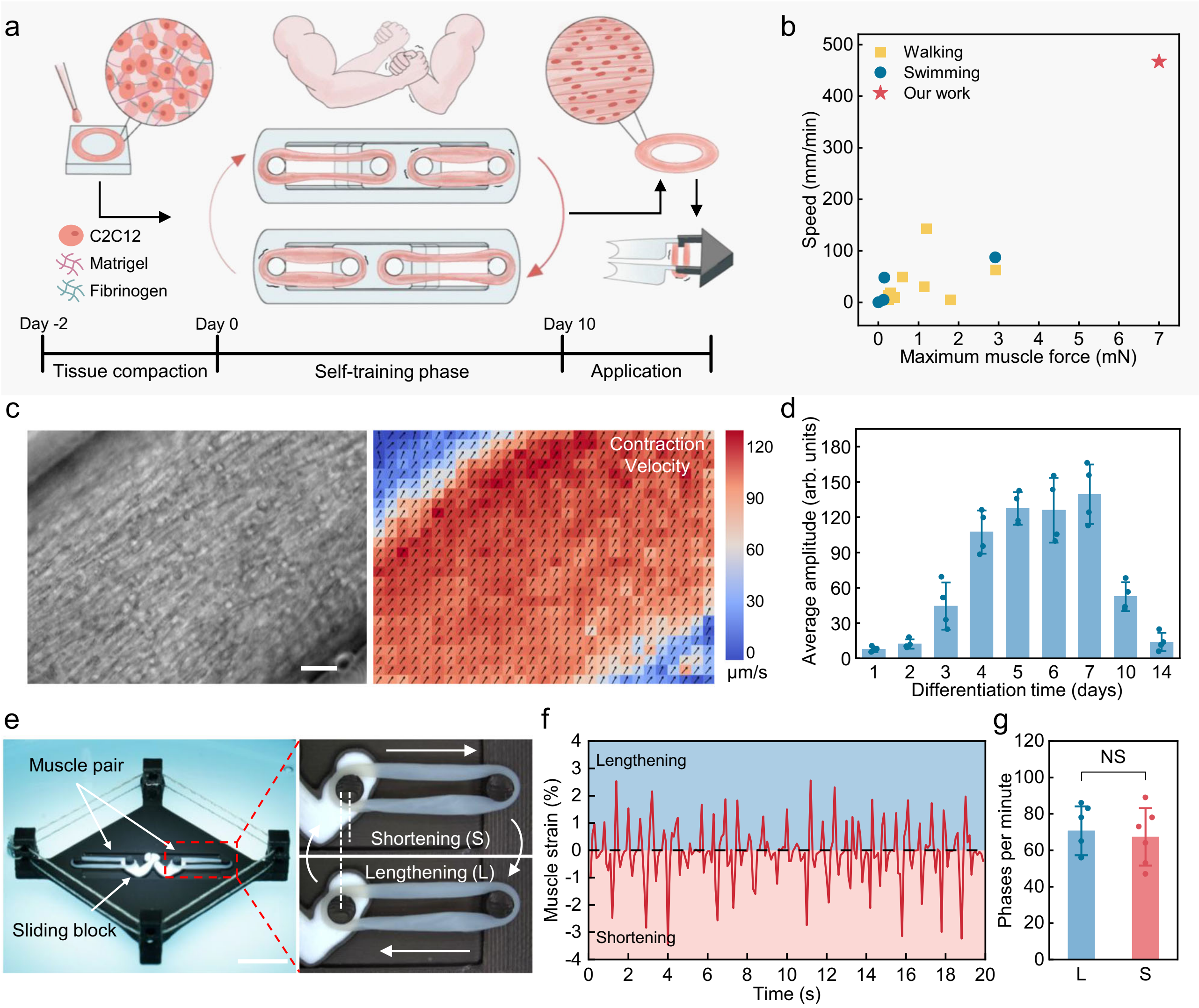

Fig. 1 | Self-training mechanism. a Conceptual illustration of the muscle tissue fabrication process using the arm-wrestling-inspired self-training platform. **b** Benchmarking of biohybrid robot performance in terms of maximum muscle force and locomotion speed. **c** Microscopic image of the C2C12 muscle tissue (left) and corresponding contraction velocity map (right) at day 4 of differentiation. Scale bar, 100 μm. **d** Evolution of average spontaneous contraction amplitude across differentiation days ($n = 4$). **e** Images showing the self-training platform (left), shortening phase and lengthening phase (right) during self-training. Scale bar, 10 mm. **f** Muscle strain profile during self-training. **g** Number of lengthening and shortening phases per minute experienced by the muscles during self-training ($n = 6$). Significance was determined using two-tailed Student's *t*-test ($P = 0.70194$, NS represents not significant). Data represent mean ± SD.

Movie 1). This evolution coincided with key morphological changes of the muscle tissues (Supplementary Fig. 2), with spontaneous twitching diminishing after day 7 as myotube formation and maturation progressed. This spontaneous contractile activity created a natural time window for autonomous self-training during early muscle development, precisely when mechanical stimulation is most effective for promoting myotube alignment and hypertrophy[35]. Conveniently, as the muscle tissues matured and spontaneous twitching subsided, they transitioned into a stable state well-suited for externally controlled robotic actuation.

With the robust spontaneous contraction as the driving force, the proposed self-training platform translated this activity into reciprocal mechanical interactions between the paired muscle tissues. Analogous to an arm-wrestling contest, the spontaneous contraction of one muscle exerted a pulling force that lengthened its counterpart. In turn, contractions from the opposing muscle generated reciprocal loading, resulting in continuous alternating lengthening–shortening strain cycles across the muscle pair without the need for external mechanical input (Fig. 1e, Supplementary Movie 2). The maximum strain experienced by a single muscle during these cycles was approximately ± 2.8% (peak to peak ~ 5.6%), which emerged spontaneously from force balance between the paired muscles rather than from externally imposed displacement (Fig. 1f). Notably, our self-training platform enabled balanced mechanical training within the muscle pair: each tissue experienced a similar number of shortening and lengthening phases per minute with no significant differences (Fig. 1g). After 7 days of differentiation, both muscles maintained comparable resting lengths (Supplementary Fig. 3), further confirming that the platform provided balanced and consistent mechanical stimulation throughout the self-training phase.

Importantly, the spontaneous contraction activity of C2C12 muscle tissues was consistently observed across batches when standard protocols were followed, confirming the reliability and reproducibility of our self-training mechanism (Supplementary Movie 3). Similar spontaneous contractility has also been reported in both C2C12-derived[23,36–38] and primary myoblast-based muscle constructs[39–43], further supporting its generalizability and robustness as a force enhancement strategy. Moreover, we observed effective self-training across muscle constructs of different sizes, highlighting the scalability of this approach (Supplementary Movie 4).

Enhanced contractile performance of self-trained skeletal muscles

To evaluate the effect of proposed self-training on muscle maturation and force generation, we compared the proposed self-training maturation platform (STMP) with two control configurations (Supplementary Fig. 4). The low stiffness maturation platform (LMP) represensts the most commonly adopted maturation configuration in biohybrid robotic systems, in which muscle tissues are differentiated while attached to a compliant skeleton that permits actuation but provides limited mechanical support during maturation. This condition captures the trade-off between structural compliance and force development that constrains most existing biohybrid robots. The high-stiffness maturation platform (HMP) was introduced as an internal control to isolate the effect of self-training. In this configuration, the muscles were fixed between rigid posts to suppress self-induced length change while providing enhanced mechanical support. To assess and compare structural maturation of skeletal muscle tissues, we performed immunofluorescence staining for myosin heavy chain and nuclei (Fig. 2a) and further visualized the images with line integral convolution (Fig. 2b). Muscle tissues cultured on the LMP exhibited disorganized myotube formation with poor alignment (Fig. 2a(i)), while those matured on the HMP showed better alignment but still contained regions of misalignment and non-uniform fiber thickness (Fig. 2a(ii)). In contrast, tissues cultured on the STMP displayed highly aligned, densely packed myotubes (Fig. 2a(iii)). Notably, high-magnification imaging revealed clear sarcomeric striations within the STMP-cultured tissues (Fig. 2a(iv)), indicating advanced structural maturation and sarcomere organization[44]. Furthermore, quantitative orientation analysis revealed that STMP-cultured muscle tissues exhibited a sharp, narrow peak around 0°, indicating highly aligned myotube organization. In contrast, HMP-cultured tissues showed a broader distribution concentrated within 0–15°, suggesting moderate alignment, while LMP-cultured tissues displayed a widely dispersed orientation profile with no distinct directional preference (Fig. 2c). Myotube diameter analysis revealed the largest average diameters in the STMP group (~ 20 μm), followed by the LMP group (~ 16 μm), with the HMP group showing significantly smaller diameters (~ 10 μm) (Fig. 2d), indicating greater fiber hypertrophy after self-training. Importantly, although myotubes in the LMP group exhibited a larger average diameter than those in the HMP, LMP-cultured tissues showed inferior force output due to poor global alignment, which limits efficient summation of myotube contractile forces at the tissue level.

To assess functional performance, we used an ultrasensitive force transducer to directly measure the active force output of the muscle tissues under varying stimulation frequencies. The force generation profile closely followed the stimulation frequency, with force summation occurring at increasing frequencies and full tetanus when above 20 Hz (Supplementary Fig. 5). For STMP-cultured muscle pair, the left and right tissues produced comparable active force amplitudes and activation profiles (Supplementary Fig. 6), further confirming balanced training shown in Fig. 1g. Across all stimulation frequencies tested, muscle tissues matured on the STMP generated significantly higher active forces compared to those on the HMP and LMP (Fig. 2e). Under 20 Hz stimulation, the STMP-cultured muscle tissues achieved peak tetanic forces of ~ 6.15 ± 0.67 mN, whereas the HMP and LMP tissues produced maximum forces around 3.70 ± 0.41 mN and 0.86 ± 0.18 mN, respectively. To further assess the durability of the muscle contractility, we monitored active forces over 21 days (Fig. 2f). Both the STMP and HMP groups showed a similar trend of increasing active force during early differentiation, peaking around day 12, and remaining relatively stable without significant decline until day 17. However, the STMP group consistently exhibited higher active forces compared to the HMP group. Notably, on day 4, the active forces of STMP and HMP were at similar levels, but the STMP group showed a markedly larger increase in force thereafter. This suggests that the self-training contributed to enhanced strengthening starting from day 4, coinciding with the onset of robust spontaneous contraction activity. In contrast, the LMP group displayed an early force peak at day 7, followed by a continuous decline until day 21, when many samples ruptured due to excessive passive tension buildup. LIVE/DEAD staining performed at day 21 revealed that STMP-cultured muscle tissues exhibited predominantly live cells with minimal dead cell presence at the tissue surface and near-surface regions (Supplementary Fig. 7). While this imaging does not directly assess cell viability in the tissue core, the STMP tissues maintained consistent and strong force output at day 21 (Fig. 2f), indicating sustained contractile function over long-term culture. These results collectively demonstrate that the STMP platform not only enhances structural maturation but also significantly improves functional contractility and long-term durability of engineered skeletal muscle tissues. The differences in contractile performance among the three platforms can be attributed to their distinct spontaneous contraction profiles (Supplementary Fig. 8). On the HMP, the high stiffness restrains muscle contractions, limiting the magnitude of mechanical stimulation; on the LMP, although the compliant beams allowed larger spontaneous contractions, the progressively increasing passive tension caused the muscle length to shorten over time, leading to loss of structural integrity (Supplementary Fig. 9). In contrast, the STMP provided a dynamic equilibrium of developing passive forces between the muscle pair, maintaining muscle length

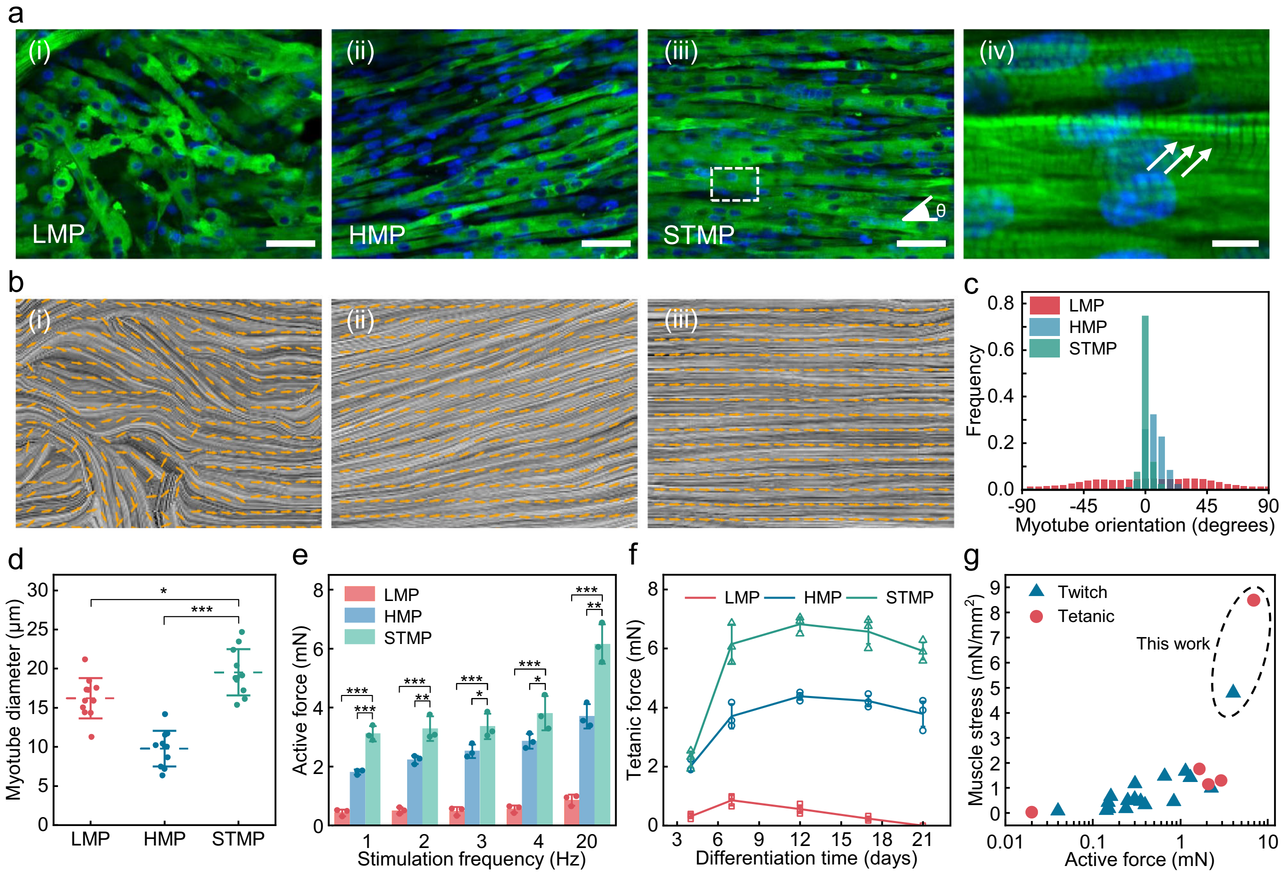

Fig. 2 | Functional evaluation of muscle tissues cultured on different maturation platforms. a Immunostaining images of muscle tissues cultured on (i) LMP, (ii) HMP, (iii) STMP, and (iv) a high-magnification view of the STMP-cultured muscle tissue highlighting sarcomeric striations (indicated by three arrows) at day 7. Green: myosin heavy chain; blue: nuclei. θ denotes the myotube orientation angle relative to the longitudinal axis of the construct. Scale bars, (i-iii) 50 µm; (iv) 10 µm. **b** Alignment visualization using line integral convolution mapped with orientation vector fields of muscle tissues cultured on (i) LMP, (ii) HMP, (iii) STMP. **c** Frequency distribution plots of myotube orientations. **d** Quantification of myotube diameters ($n = 11$). **e** Active force generation under electrical stimulation at day 7 ($n = 3$). **f** Evolution of muscle tetanic forces over time ($n = 3$). **g** Comparison of twitch/tetanic forces and stresses for self-trained muscles versus previously reported C2C12 muscle tissues. Significance was determined using Tukey's post hoc test (*$P < 0.05$, **$P < 0.01$, and ***$P < 0.001$). Data represent mean ± SD.

under built-up tensions while enabling large spontaneous contraction amplitude for self-training.

To contextualize these findings within the broader field of biohybrid robotics, we benchmarked the contractile performance of our self-trained muscle actuators against previously reported C2C12-based systems, using both absolute force and normalized muscle stress as metrics. Cross-sectional areas, measured from hematoxylin and eosin (H&E)–stained sections, averaged 0.83 ± 0.15 mm^2 (Supplementary Fig. 10). From these values, the STMP-cultured muscles produced maximum twitch and tetanic forces of 4.21 mN (5.08 mN/mm^2) and 7.05 mN (8.51 mN/mm^2), respectively—both substantially higher than those reported for muscle actuators in prior biohybrid robot studies[7–9,14,19,21,23,26–30,32,45–47] (Fig. 2g, Supplementary Table 2), underscoring the ability of the self-training platform to overcome the longstanding low force generation bottleneck in this field.

Model-informed design of a twin-tail biohybrid swimming robot

To showcase the capabilities of the self-trained high-force muscle tissues, we designed a twin-tail biohybrid swimming robot—OstraBot. This design was inspired by the ostraciiform swimming of boxfish, a mode of locomotion distinct from the undulatory swimming used by most swimming robots[48–50], which involves coordinated body and tail motion. In ostraciiform swimming, the body remains rigid while thrust is generated solely by oscillating the tails[51], resulting in a mechanically simple structure capable of stable, energy-saving propulsion[52], features that are well-suited for biohybrid actuation. OstraBot consists of a rigid body for stabilization, a self-trained muscle as the driving force, a pair of flexible beams functioning as artificial tendons for force transmission, and two tails for propulsion (Fig. 3a). Upon electrical stimulation, the muscle contracts, deforming the artificial tendons and driving oscillatory motion of the tails to propel the robot forward.

Achieving high robotic performance requires not only strong muscle actuators but also a rational system design. To this end, we mechanically represented the biohybrid robot as an active muscle element connected to a linear elastic spring, representing the artificial tendon, and a viscous damper, representing the hydrodynamic drag (Fig. 3b). The mechanical properties of the spring and damper can be determined experimentally: force–deflection testing of the tendon beams confirmed highly linear bending behavior under small deflections (Fig. 3c), allowing modeling as a linear spring, while the damping coefficient could be obtained by fitting to experimental motion data. In contrast, the muscle actuator is inherently more challenging to model due to its dynamic and nonlinear force-generating characteristics[53]. In many biohybrid robot studies, the complexity of muscle behavior is simplified by approximating the muscle as a linear actuator[54].

To better account for underlying muscle dynamics in robotic design and control, we developed a physiology-based contraction model that link electrical stimulation to force output through four interconnected biological stages: electric flux, calcium dynamics, muscle activation, and crossbridge cycling (Fig. 3d). Each stage is

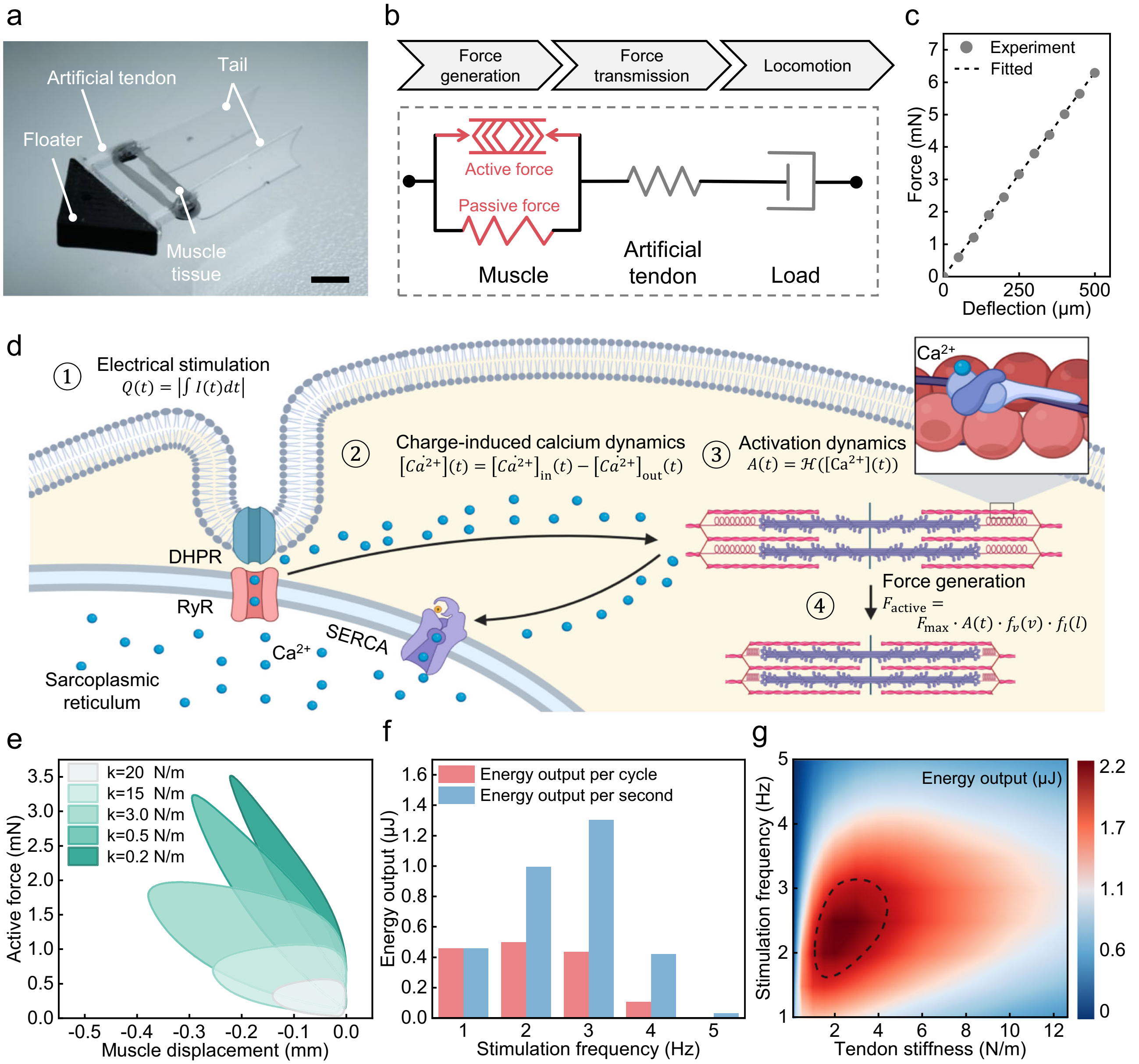

Fig. 3 | Model-informed design of a biohybrid OstraBot. a Image of the fabricated biohybrid OstraBot. Scale bar, 5 mm. **b** Mechanical representation of the biohybrid system. **c** Measured force–deflection relation of the artificial tendon. **d** Schematic illustration of the physiological processes underlying skeletal muscle force generation in vitro. Image created with BioRender. **e** Simulated active force–displacement loops in a single contraction-relaxation cycle at 3 Hz stimulation. Tendon stiffness was varied as indicated; shaded area denotes the mechanical work (energy output) per cycle. **f** Simulated muscle energy output per cycle and per second under different stimulation frequencies, with tendon stiffness fixed at $k = 3.0$ N/m. **g** Heatmap of simulated muscle energy output with different tendon stiffness and stimulation frequency combinations.

described by a set of differential equations[55–57] (see Supplementary Note 1 for detailed derivations), enabling the model to take an input electrical stimulation signal, solve the resulting calcium and activation dynamics, and predict the complete time course of muscle force generation. In the contraction model, the active force generated by the skeletal muscle is governed by:

$$F_{active} = F_{max} \cdot A(t) \cdot f_v(v) \cdot f_l(l) \tag{1}$$

where F_{max} is the maximum isometric force that the muscle can generate, $A(t)$ is the stimulation-dependent activation level. $f_v(v)$ and $f_l(l)$ represent the force–velocity and force–length scaling functions, respectively. These two terms account for the inverse relationship between contraction velocity and force (Supplementary Fig. 11a) and the muscle's optimal length range (Supplementary Fig. 11b). The scaling functions are independent and can be calibrated separately from force measurements under specific testing conditions (see Supplementary Note 2 for model calibration). Simulation results of the calibrated model closely matched experimental measurements (Supplementary Fig. 12a), reproducing peak force, stimulation-dependent contraction frequency, and key temporal features such as time to peak tension and half-relaxation time (Supplementary Fig. 12b), demonstrating its capability to accurately simulate the amplitude and dynamic profile of muscle force generation.

We then integrated the muscle contraction model into the muscle–tendon–load framework of the OstraBot to predict the robot's performance (see Supplementary Note 3). For the robot to achieve high performance, the muscle should produce the greatest possible

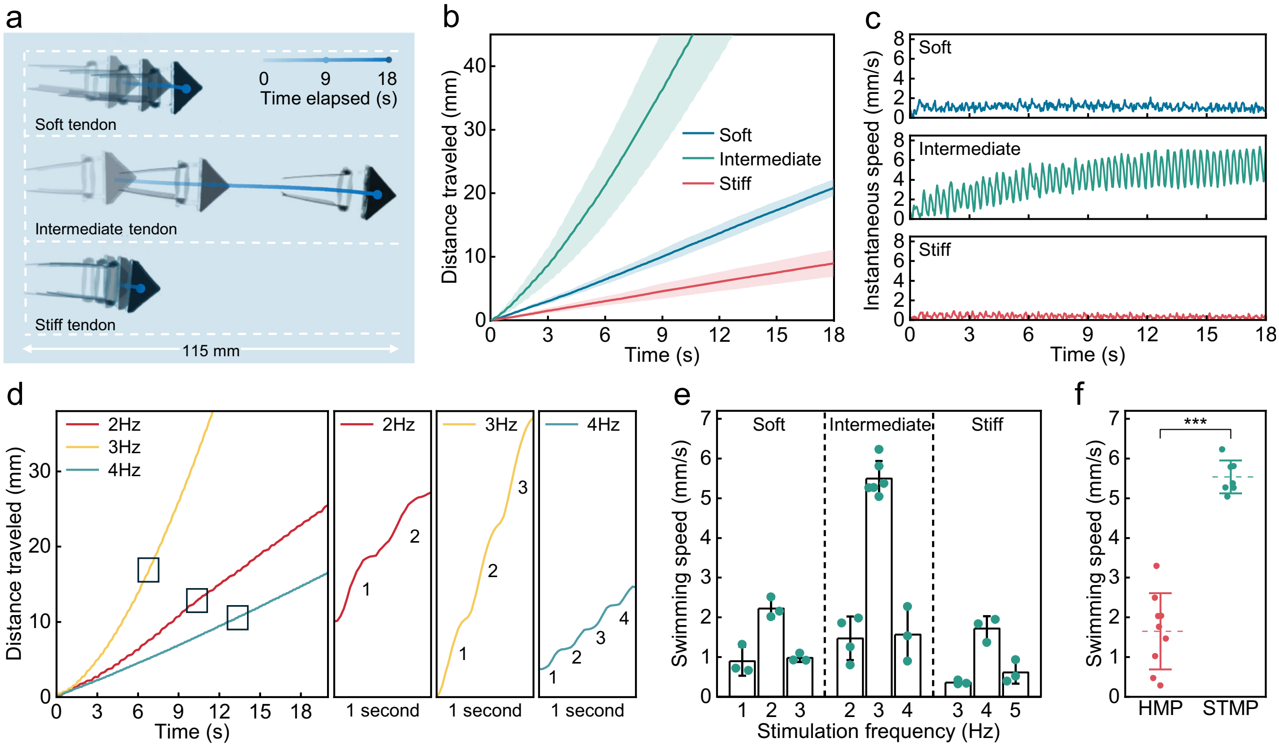

Fig. 4 | Swimming performance of OstraBot with different tendon stiffness and stimulation frequencies. Swimming trajectories and quantitative analysis of OstraBots with different tendon stiffness at 3 Hz stimulation: **a** top-view composite trajectories, **b** distance–time profiles ($n = 3$ independent muscles per robot), and **c** instantaneous swimming speeds. **d** Distance–time profiles of the intermediate-tendon OstraBots stimulated at 2 Hz, 3 Hz, and 4 Hz. **e** Steady-state swimming speed of OstraBot with varying stiffness–frequency combinations ($n = 3$–5 independent muscles per robot). **f** Swimming speed comparison of OstraBots powered by HMP- and STMP-cultured muscles (HMP: $n = 9$; STMP: $n = 7$; $P = 0.0000001$). Significance was determined using two-tailed Student's *t*-test (***$P < 0.001$). Data represent mean ± SD.

mechanical work in each contraction-relaxation cycle (Supplementary Fig. 13). Because the tendon always returns to its starting position, no elastic energy is stored between cycles; thus, in this idealized scenario, the muscle's energy output is directly translated into robotic motion. Tendon stiffness is a key parameter governing the muscle's energy output, as it determines how the muscle responds dynamically and how effectively muscle forces are transmitted. Similar to biological tendons, an appropriate tendon stiffness balances energy storage, force transmission, and overall efficiency[58–60]. Model simulations revealed that tendons that are too stiff limit deformation and produce minimal motion, while overly soft tendons allow large deformations but insufficient restoring force to complete the cycle, reducing useful work. Only tendons with intermediate stiffness produce the largest energy loop areas, indicating maximal mechanical work generation (Fig. 3e, Supplementary Fig. 14). In addition to tendon stiffness as a structural design parameter, stimulation frequency serves as a key operational control parameter influencing system performance. For a single contraction-relaxation cycle, higher stimulation frequencies lead to contraction summation, which reduces the mechanical energy output per cycle (Supplementary Fig. 15). When total energy output over time is considered, however, a stimulation frequency of 3 Hz yielded the highest simulated performance for tendons of intermediate stiffness, balancing energy per cycle with cycle repetition rate (Fig. 3f).

To examine the combined influence of tendon stiffness and stimulation frequency, we generated a heatmap of muscle energy output across varying stiffness–frequency combinations (Fig. 3g). We defined a high-performance range as the region where energy output exceeded 80% of the maximum, indicated by the overlaid circle. The simulation reveals a distinct tendon stiffness range of 1.0–4.5 N/m associated with maximal energy output. Interestingly, the simulation uncovered a stiffness–frequency matching phenomenon: softer tendons performed best at lower stimulation frequencies, whereas stiffer tendons benefited from higher stimulation frequencies. These simulation results highlight how both tendon stiffness (design parameter) and stimulation frequency (control parameter) can be tuned in concert to enhance biohybrid robot performance.

Experimental validation of stiffness design and frequency matching

To validate the simulation predictions, we fabricated OstraBot variants with soft, intermediate, and stiff tendons with stiffness values of 0.77 N/m, 2.88 N/m, and 12.64 N/m, respectively (Supplementary Fig. 16). At a stimulation frequency of 3 Hz, the self-trained muscle under STMP contracted robustly, producing oscillatory tail motion that propelled the robots forward. Swimming performance varied markedly with tendon stiffness. The intermediate-stiffness OstraBot achieved the greatest displacement, consistently outperforming both the soft- and stiff-tendon designs (Fig. 4a, Supplementary Movie 5). Quantitative displacement measurements (Fig. 4b) confirmed these trends: the intermediate-stiffness robot traveled 80.22 mm over 18 s, reaching a steady-state speed of 5.50 mm/s, compared to 20.09 mm (0.98 mm/s) for the soft-tendon design and 7.98 mm (0.36 mm/s) for the stiff-tendon design. Interestingly, only the intermediate-stiffness OstraBot exhibited a distinct acceleration phase, as seen in the displacement-time profiles and confirmed by instantaneous speed measurements (Fig. 4c). In each actuation cycle, the muscle accelerated the robot to a sufficiently high instantaneous speed to prevent a complete stop, thereby allowing momentum to accumulate over time. In contrast, the soft- and stiff-tendon OstraBots attained lower peak speeds and halted between actuation cycles, which precluded forward momentum buildup. Muscle displacement tracking (Supplementary Fig. 17) provided a mechanistic explanation consistent with model predictions: when the tendon was too soft, the tail oscillated over a small angular range despite large absolute displacement, producing limited effective thrust, whereas the stiff-tendon design generated minimal displacement due to restricted beam deformation, also resulting in low thrust.

We next examined how stimulation frequency, a key operational control parameter, interacts with stiffness to modulate robot swimming performance. For the intermediate-tendon OstraBot, the distance–time curves exhibited a clear stepwise pattern, with step intervals corresponding directly to the stimulation period (Fig. 4d). Stimulation at 3 Hz produced the fastest forward motion, characterized by a distinct acceleration phase (Supplementary Movie 6), whereas stimulation at 2 Hz and 4 Hz resulted in significantly slower motion with no evident speed accumulation across actuation cycles. When performance was compared across all stiffness groups, a clear stiffness–frequency matching pattern emerged: for the soft-tendon robot, the highest speed (~2.23 mm/s) occurred at 2 Hz (Supplementary Movie 7), whereas with increasing tendon stiffness, the frequency yielding peak speed also increased. The intermediate-stiffness robot reached its maximum speed (~5.50 mm/s) at 3 Hz, while the stiff-tendon robot performed best (~1.72 mm/s) at 4 Hz (Fig. 4e). These findings demonstrate that matching actuation frequency to tendon stiffness is essential for maximizing biohybrid robot performance, in agreement with predictions from our muscle–tendon interaction model.

Finally, to showcase the importance and necessity of strong muscle actuators for achieving high performance, we compared OstraBot powered by HMP- and STMP-cultured muscles. The STMP-powered robot swam more than three times faster than its HMP-powered counterpart (Fig. 4f, Supplementary Movie 8), highlighting how increasing muscle force directly translates to improved biohybrid robot performance.

Demonstration of controllability and robust operation

Having validated how structural design and actuation control influence swimming performance, we next performed additional demonstrations to assess OstraBot's controllability. While swimming speed can be tuned by stimulation frequency, this simultaneously alters stroke timing and the overall swimming pattern. In contrast, varying the electric field strength provides a more direct and continuous means of speed modulation by controlling muscle activation levels, without altering the underlying kinematics of the swimming motion. Increasing the field strength from 0.15 V/mm to 0.50 V/mm progressively enhanced swimming speed, whereas further increasing it to 0.70 V/mm resulted in a marked reduction (Fig. 5a, b, and Supplementary Movie 9). This decrease is likely due to overstimulation effects such as excessive charge accumulation, ionic imbalance, or early-onset muscle fatigue[61], all of which can impair contractile performance. The maximum swimming speed reached 7.78 mm/s (0.26 body length/s) when stimulated at 0.50 V/mm and 3 Hz (Fig. 5c). We further assessed OstraBot's robustness by introducing external disturbances during steady forward swimming. When momentarily pushed backward, the robot exhibited a brief reversal in displacement and a transient negative swimming speed (Fig. 5d). It rapidly regained forward motion within a few seconds (Fig. 5e), demonstrating strong recovery capability and resilience to mechanical interference. This rapid recovery is attributed to the system's high thrust generation, enabled by the strong contractile output of the self-trained muscles and the model-informed mechanical design of the robot.

To further demonstrate OstraBot's on–off controllability, we constructed a sound-triggered control system that activated and deactivated swimming in response to clapping signals (Supplementary Fig. 18). The robot was programmed to start swimming upon detecting two consecutive claps and to stop when a single clap was detected. In the absence of sound signals, the robot remained stationary. Upon receiving the start command, electrical stimulation was applied to the muscle actuator, and the robot immediately initiated swimming. Upon receiving the stop command, stimulation ceased, tail oscillations stopped, and the robot glided for about 4 s before halting completely (Fig. 5f, Supplementary Movie 10). Notably, while these engineered muscles exhibit spontaneous contractions during early development, their amplitude diminishes substantially and the activity becomes random by the time they are integrated into the robot (Fig. 5g). As a result, spontaneous contractions cannot generate continuous thrust to overcome hydrodynamic resistance, ensuring precise on–off control of the robot.

Discussion

To address the long-standing performance bottleneck in biohybrid robot research, we developed a self-training platform exploiting the robust spontaneous contraction behavior of engineered skeletal muscle tissues. This system allows the muscle tissues to autonomously train against one another through continuous shortening–lengthening cycles, without requiring specialized equipment or manual intervention. Using this self-training strategy, we achieved a maximum active force of ~ 7.05 mN (8.51 mN/mm^2) with C2C12 cell lines, significantly exceeding previously reported values for this cell line in biohybrid robots and comparable to those engineered from primary cells[13]. This approach provides a simple yet robust method to fabricate high-strength skeletal muscle tissues, offering reliable biological actuator sources for future biohybrid systems.

More broadly, the enhanced force output achieved using the STMP can be attributed to several defining features of the training strategy. The platform enables a maturation-then-assembly approach, decoupling muscle differentiation from the mechanical constraints of the final robotic skeleton and thereby overcoming the stiffness trade-off that limits force development in conventional biohybrid systems. In addition, the STMP establishes a dynamically balanced mechanical environment by pairing muscles with reciprocal mechanical opposition. Unlike low-stiffness platforms that allow contraction but lead to progressive muscle shortening, or rigid platforms that maintain muscle length while suppressing movement, deformation in the STMP emerges naturally from force balance between opposing muscles coupled through the sliding block. Finally, mechanical stimulation in the STMP is contraction-driven and bidirectional, encompassing both shortening and subsequent lengthening phases. Although the instantaneous strain amplitude experienced by individual muscles is relatively modest (±2–3%), this force-regulated stimulation is applied continuously and adjusts naturally as muscle force develops. This self-training configuration differs fundamentally from displacement-controlled systems that impose intermittent, externally prescribed strain[62].

To demonstrate the potential of the self-trained high-strength muscles, we designed a twin-tail biohybrid swimming robot, OstraBot, inspired by the stable and energy-saving ostraciiform swimming of boxfish. The design was guided by our physiology-based muscle contraction model, which identified an optimal tendon stiffness range and a stiffness–frequency matching phenomenon to enhance performance. Notably, this stiffness–frequency matching behavior is consistent with prior studies in aquatic locomotion[63], in which frequency-dependent body or appendage stiffness has been shown to play a key role in efficient propulsion in both biological swimmers and bioinspired robotic systems[64–66]. By combining the strong muscles with this model-informed design, OstraBot achieved a swimming speed of 467 mm/min, the fastest reported for skeletal muscle–driven biohybrid robots, while maintaining precise controllability.

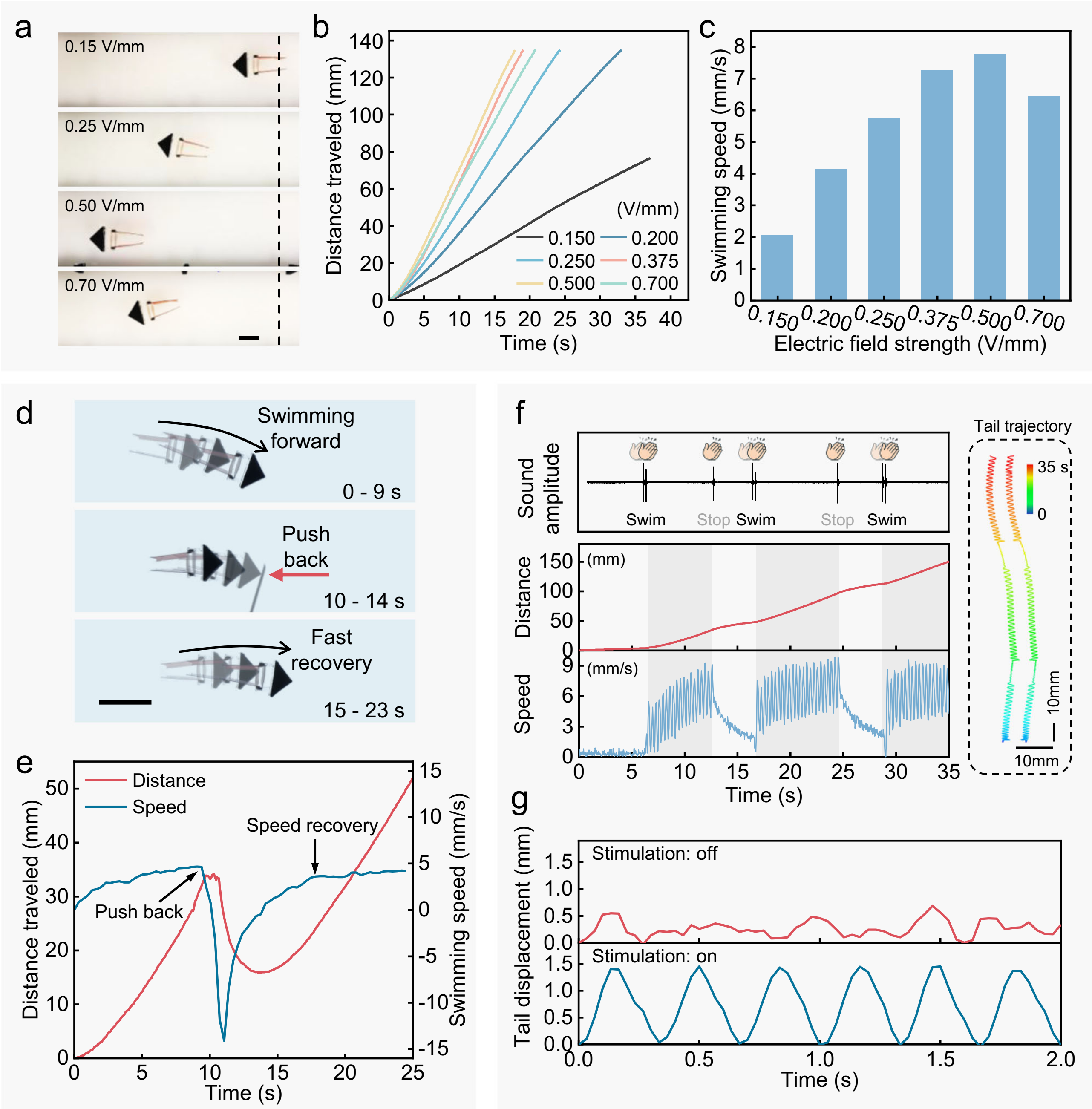

Fig. 5 | Speed modulation and on–off control of OstraBot. a Top view images showing OstraBot positions after 15 seconds under different electric field strengths (3 Hz stimulation). Dash line indicates the starting position. Scale bar, 10 mm. Quantitative performance at different electric fields: **b** traveling distance and **c** steady-state swimming speed. **d** Composite top view trajectories showing the speed recovery after external interference. Scale bar, 20 mm. **e** Traveling distance and swimming speed of OstraBot under interference. **f** On–off control using clapping signals: traveling distance and instantaneous speed (left) and corresponding tail trajectory (right). **g** Tail displacement amplitude before and after applying electrical stimulation.

Despite these advances, further improvements in swimming efficiency remain an important direction for biohybrid robotic systems. While overcoming the force-output bottleneck is a necessary prerequisite for high-performance locomotion, swimming efficiency is a system-level property governed by additional factors such as tail size, tail geometrybody, and overall body morphology. Recent studies have shown that jointly optimizing morphology and actuation using machine learning-based approaches can substantially improve swimming efficiency in biohybrid fish robots[67]. In this context, the self-trained high-strength muscles and the muscle–tendon theoretical framework established here provide a robust foundation upon which such system-level efficiency optimization can be accomplished.

Together, the self-training strategy and the predictive contraction model developed in this work not only enabled record-setting actuation force and swimming speed but, more importantly, provided a universal and accessible framework for advancing biohybrid robot design. By harnessing spontaneous contractions, the self-training approach could be readily applied to primary skeletal muscle tissues to achieve even greater force outputs, while the predictive model can be extended to simulate systems with multiple muscles, advanced skeleton designs, and high-degree-of-freedom actuation. This platform has the potential to create stronger, more efficient, and highly functional biohybrid machines across diverse applications.

Methods

Cell culture

The cells used in this study were the mouse myoblast cell line C2C12 (CRL-1772, ATCC) under passage 5. The cells were cultured and expanded in growth medium consisting of high-glucose Dulbecco's modified Eagle's medium (DMEM, Gibco) supplemented with 10% (v/v) fetal bovine serum (FBS, Gibco) and 1% penicillin-streptomycin (Gibco). The cells were passaged at a 10:1 split ratio before reaching 70% confluency to avoid depletion of differentiation potential. To induce myogenic differentiation, the culture medium was changed to differentiation medium consisting of DMEM supplemented with 10% (v/v) horse serum (HS, Gibco), 1% penicillin-streptomycin (Gibco), 50 ng/mL insulin-like growth factor (IGF-LR3-1, PeproTech), and 1 mg/mL of 6-aminocaproic acid (Sigma-Aldrich).

Formation of skeletal muscle tissues and self-training

To construct the skeletal muscle tissues, PDMS injection models were first fabricated by molding against a 3D-printed ring-shaped polylactic acid (PLA) mold using a commercial fused deposition modeling (FDM) printer (Bambu Lab X1C). Prior to cell seeding, the PDMS molds were autoclaved, plasma-treated and coated with 1% wt F-127 Pluronic solution (Sigma-Aldrich) to facilitate muscle release. C2C12 cells were trypsinized, counted, centrifuged, and resuspended in growth medium to ensure a final concentration of 1.0×10^7 cells/mL in the mixture. 18 μL of cell suspension was sequentially mixed with 100 μL of fibrinogen (8 mg/mL, Sigma-Aldrich), 30 μL of Matrigel (Corning), and 2 μL of thrombin (100 U/mL, Sigma-Aldrich). After mixing, the cell-matrix mixture was seeded into the PDMS mold and incubated at 37 °C for 30 min to initiate gelation. The crosslinked cell-matrix mixture was cultured in growth medium supplemented with 1 mg/mL 6-aminocaproic acid for 2 days, allowing it to compact and gain mechanical strength before it could be transferred.

The HMP and STMP platforms were directly 3D printed using an FDM printer with PLA filaments. The LMP platform was molded using PDMS. Two days after molding, the compacted muscle tissues were carefully lifted from the mold and transferred onto the designated maturation platforms using a customized tool. Each well was filled with 5 mL of differentiation medium per muscle tissue, with daily medium changes. To assess and visualize the spontaneous contraction of the engineered muscle tissues, their motion was recorded using an inverted optical microscope (TE2000, Nikon) fitted with an incubation chamber. The temperature was maintained at 37 °C during testing. The recorded videos were analyzed using an in-house dense optical flow-based tracking algorithm.

Immunostaining

To assess and compare myogenic differentiation and alignment across samples differentiated on different platforms, tissues were processed for immunofluorescence staining. All muscle tissues were maintained on their respective maturation platforms prior to fixation to preserve structural integrity and native alignment. Tissues were washed three times with Dulbecco's phosphate buffered saline (DPBS, Hyclone) and fixed in 4% paraformaldehyde (PFA, Bioss) for 30 min at room temperature, followed by three washes in DPBS. For immunostaining, samples were permeabilized with 0.2% (v/v) Triton X-100 in DPBS for 15 min, then washed and blocked with 2% bovine serum albumin (BSA). Muscle tissues were incubated with Alexa Fluor®−488-conjugated anti-myosin heavy chain II antibody (MF-20, eBioscience) diluted in 5% DPBS-BSA buffer and left overnight at 4 °C. After three washes to remove unbound antibodies, nuclei were counterstained with 1 μg/mL DAPI (Sigma-Aldrich), followed by washing three times with DPBS. Fluorescently labelled tissues were imaged using a laser confocal laser microscope (LSM700, Zeiss), with excitation wavelengths of 405 nm for DAPI and 488 nm for MF-20. Myotube orientation was visualized using line integral convolution and quantified using OrientationJ[68].

LIVE/DEAD staining

To evaluate the viability of the engineered skeletal muscle tissues after long-term culture, LIVE/DEAD staining was performed on day 21. Briefly, the tissues were washed three times with DPBS and incubated with a staining solution containing 2 μM calcein-AM and 4 μM ethidium homodimer-1 for 30 min at 37 °C. Due to the limited optical penetration depth in thick 3D muscle constructs, confocal imaging was performed at the tissue surface and near-surface regions using a laser scanning confocal microscope.

Cryosectioning

To determine cross-sectional areas, the self-trained muscle tissues were sectioned and stained with hematoxylin and eosin. Following fixation as described above, samples were sequentially immersed in 30%, 50%, and 70% sucrose solutions at 4 °C for cryoprotection. The tissues were then embedded in optimal cutting temperature (OCT) compound, rapidly frozen in liquid nitrogen, and stored at −80 °C until sectioning. Transverse sections (10 μm thick) were prepared using a cryostat (CryoStar NX50, Thermo Fisher Scientific).

Muscle force measurement

To accurately characterize the passive and active force generated by the muscle tissues, we built a customized force-measuring device (Supplementary Fig. 19). The measuring device was composed of an ultrasensitive force transducer (LSB200-10g, FUTEK) fitted with a 3D-printed adapter for anchoring muscle tissues and a pair of carbon electrodes for electrical stimulation. The force sensor was factory calibrated and independently validated using known weights prior to experiments (Supplementary Fig. 20). Electrical signals were generated using a stimulator (Master-9, AMPI), amplified by a high-power operational amplifier (OPA541, Texas Instruments), and delivered through two platinum wires.

When measuring the active force, muscle tissues were released from the maturation platforms, placed in Tyrode's salt solution (Sigma-Aldrich), and connected to the force transducer via the adapter. When electrically stimulated, the tested muscle contracted, pulled the adaptor and transmitted the force to the transducer. The sampling rate of the transducer was set to 100 samples/second, and the average of a 5 s continuous measurement was taken as the final result.

For all electrical stimulation experiments carried out in this study, the pulse width was set to 20 ms and the electric field set to 0.25 V/mm unless specified.

Construction of the biohybrid OstraBot

The body of the OstraBot was fabricated using a FDM 3D printer (Bambu Lab X1C) with PLA filaments. The infill density was set to 20%, achieving an approximate density of 0.7 g/mm^3 to provide sufficient buoyancy. The flexible beams were made of PDMS cast in 3D-printed molds, with stiffness tuned by varying both the beam geometry (Supplementary Fig. 21) and the precursor-to-curing-agent ratios (8:1 for stiff, 10:1 for intermediate, and 20:1 for soft tendons). The tails were cut from a 0.25 mm-thick polyimide film using an automated cutting machine (Cameo 4, Silhouette). All components were assembled using medical-grade adhesive (Loctite 4861, Henkel). Before muscle integration, the robot skeleton was sterilized in 70% ethanol for 30 min and exposed to UV light for an additional 30 min. Engineered skeletal muscle tissue was then mounted onto the robot by securing it around the muscle anchors. To initiate swimming, biphasic square-wave pulses (pulse width: 20 ms) with different electric field strength were applied and delivered through a pair of parallel carbon electrodes submerged in the buffer medium.

The motion of the OstraBots was recorded using a digital camera and analyzed for swimming speed, tail beat amplitude, and frequency using Tracker software.

Statistical analysis

Statistical analysis was performed using OriginPro software. For comparisons between two groups, an unpaired two-tailed Student's *t*-test was used. For comparisons involving three groups, a one-way ANOVA followed by Tukey's post hoc test was performed. Results are presented as means ± SD. The *F* and *P* values of Fig. 2d, e are listed in Supplementary Table 3.

Data availability

All data generated or analyzed during this study are included in the Article and its Supplementary Information. The quantitative data underlying all figures are provided in the Source Data file. Source data are provided with this paper.

References

1. Ricotti, L. et al. Biohybrid actuators for robotics: a review of devices actuated by living cells. *Sci. Robot.* **2**, eaaq0495 (2017).
2. Lee, K. Y. et al. An autonomously swimming biohybrid fish designed with human cardiac biophysics. *Science* **375**, 639–647 (2022).
3. Park, S. J. et al. Phototactic guidance of a tissue-engineered soft-robotic ray. *Science* **353**, 158–162 (2016).
4. Appiah, C. et al. Living materials herald a new era in soft robotics. *Adv. Mater.* **31**, 1807747 (2019).
5. Somers, S. M., Spector, A. A., DiGirolamo, D. J. & Grayson, W. L. Biophysical stimulation for engineering functional skeletal muscle. *Tissue Eng. Part B* **23**, 362–372 (2017).
6. Raman, R., Cvetkovic, C. & Bashir, R. A modular approach to the design, fabrication, and characterization of muscle-powered biological machines. *Nat. Protoc.* **12**, 519–533 (2017).
7. Cvetkovic, C. et al. Three-dimensionally printed biological machines powered by skeletal muscle. *Proc. Natl. Acad. Sci. USA* **111**, 10125–10130 (2014).
8. Raman, R. et al. Optogenetic skeletal muscle-powered adaptive biological machines. *Proc. Natl. Acad. Sci. USA* **113**, 3497–3502 (2016).
9. Kim, Y. et al. Remote control of muscle-driven miniature robots with battery-free wireless optoelectronics. *Sci. Robot.* **8**, eadd1053 (2023).
10. Morita, T., Nie, M. & Takeuchi, S. Tetanus-driven biohybrid multijoint robots powered by muscle rings with enhanced contractile force. *Sci. Adv.* **11**, eadu9962 (2025).
11. Bartolucci, A. et al. Monolithic biohybrid flexure mechanism actuated by bioengineered skeletal muscle tissue. *Adv. Intell. Syst.* 2400989, https://doi.org/10.1002/aisy.202400989 (2025).
12. Ren, X., Morimoto, Y. & Takeuchi, S. Biohybrid hand actuated by multiple human muscle tissues. *Sci. Robot.* **10**, eadr5512 (2025).
13. Morimoto, Y., Onoe, H. & Takeuchi, S. Biohybrid robot powered by an antagonistic pair of skeletal muscle tissues. *Sci. Robot.* **3**, eaat4440 (2018).
14. Yang, H. et al. Modular assembly of biohybrid machines using force-enhanced skeletal muscle actuators. Preprint at https://www.biorxiv.org/content/10.1101/2025.07.06.663299 (2025).
15. Kinjo, R., Morimoto, Y., Jo, B. & Takeuchi, S. Biohybrid bipedal robot powered by skeletal muscle tissue. *Matter* **7**, 948–962 (2024).
16. Rao, L., Qian, Y., Khodabukus, A., Ribar, T. & Bursac, N. Engineering human pluripotent stem cells into a functional skeletal muscle tissue. *Nat. Commun.* **9**, 126 (2018).
17. Machida, S., Spangenburg, E. & Booth, F. Primary rat muscle progenitor cells have decreased proliferation and myotube formation during passages. *Cell Prolif.* **37**, 267–277 (2004).
18. Reid, G., Magarotto, F., Marsano, A. & Pozzobon, M. Next stage approach to tissue engineering skeletal muscle. *Bioengineering* **7**, 118 (2020).
19. Wang, X., Schirmer, C., Totter, E. & Schuerle, S. Microalgae empower skeletal muscle via increased force production and viability. *Sci. Adv.* **11**, eadw5786 (2025).
20. Mestre, R. et al. Force modulation and adaptability of 3D-bioprinted biological actuators based on skeletal muscle tissue. *Adv. Mater. Technol.* **4**, 1800631 (2019).
21. Yang, L. et al. Dynamic electromechanical co-stimulation based enhancement of skeletal muscle tissues for fast biosyncretic robots actuation. *Adv. Funct. Mater.* **35**, 2410334 (2025).
22. Jo, B., Motoi, K., Morimoto, Y. & Takeuchi, S. Dynamic and static workout of in vitro skeletal muscle tissue through a weight training device. *Adv. Healthc. Mater.* **13**, 2401844 (2024).
23. Guix, M. et al. Biohybrid soft robots with self-stimulating skeletons. *Sci. Robot.* **6**, eabe7577 (2021).
24. Wang, J. et al. Engineered skeletal muscles for disease modeling and drug discovery. *Biomaterials* **221**, 119416 (2019).
25. Mueller, C. et al. Effects of external stimulators on engineered skeletal muscle tissue maturation. *Adv. Mater. Interfaces* **8**, 2001167 (2021).
26. Pagan-Diaz, G. J. et al. Simulation and fabrication of stronger, larger, and faster walking biohybrid machines. *Adv. Funct. Mater.* **28**, 1801145 (2018).
27. Wang, J. et al. Computationally assisted design and selection of maneuverable biological walking machines. *Adv. Intell. Syst.* **3**, 2000237 (2021).
28. Wang, J., Wang, Y., Kim, Y., Yu, T. & Bashir, R. Multi-actuator light-controlled biological robots. *APL Bioeng.* **6**, 036103 (2022).
29. Mestre, R. et al. Improved performance of biohybrid muscle-based bio-bots doped with piezoelectric boron nitride nanotubes. *Adv. Mater. Technol.* **8**, 2200505 (2023).
30. Yang, L. et al. Modular living muscle-based biomimetic actuators for biosyncretic robots. *SmartBot* e12012, https://doi.org/10.1002/smb2.12012 (2025).
31. Aydin, O. et al. Neuromuscular actuation of biohybrid motile bots. *Proc. Natl. Acad. Sci. USA* **116**, 19841–19847 (2019).
32. Zhang, C., Zhang, Y., Wang, W., Xi, N. & Liu, L. A manta ray-inspired biosyncretic robot with stable controllability by dynamic electric stimulation. *Cyborg Bionic Syst.* 9891380, https://doi.org/10.34133/2022/9891380 (2022).
33. Balciunaite, A., Yasa, O., Filippi, M., Michelis, M. Y. & Katzschmann, R. K. Bilayered biofabrication unlocks the potential of skeletal muscle for biohybrid soft robots. In *2024 IEEE 7th International Conference on Soft Robotics (RoboSoft)* 525-530, https://doi.org/10.1109/RoboSoft60065.2024.10522009 (2024).
34. Drennan, W. C. et al. A forward-engineered, muscle-driven soft robotic swimmer. *Sci. Adv.* **11**, eadu8634 (2025).
35. Powell, C. A., Smiley, B. L., Mills, J. & Vandenburgh, H. H. Mechanical stimulation improves tissue-engineered human skeletal muscle. *Am. J. Physiol. Cell Physiol.* **283**, C1557–C1565 (2002).
36. Denes, L. T. et al. Culturing C2C12 myotubes on micromolded gelatin hydrogels accelerates myotube maturation. *Skelet. muscle* **9**, 17 (2019).
37. Manabe, Y. et al. Characterization of an acute muscle contraction model using cultured C2C12 myotubes. *PLoS ONE* **7**, e52592 (2012).
38. Cvetkovic, C. et al. Investigating the life expectancy and proteolytic degradation of engineered skeletal muscle biological machines. *Sci. Rep.* **7**, 3775 (2017).
39. Hinds, S., Bian, W., Dennis, R. G. & Bursac, N. The role of extracellular matrix composition in structure and function of bioengineered skeletal muscle. *Biomaterials* **32**, 3575–3583 (2011).
40. Bian, W. & Bursac, N. Engineered skeletal muscle tissue networks with controllable architecture. *Biomaterials* **30**, 1401–1412 (2009).
41. Madden, L., Juhas, M., Kraus, W. E., Truskey, G. A. & Bursac, N. Bioengineered human myobundles mimic clinical responses of skeletal muscle to drugs. *elife* **4**, e04885 (2015).
42. Juhas, M., Engelmayr, G. C. Jr, Fontanella, A. N., Palmer, G. M. & Bursac, N. Biomimetic engineered muscle with capacity for

vascular integration and functional maturation in vivo. *Proc. Natl. Acad. Sci. USA* **111**, 5508–5513 (2014).
43. Santoso, J. W. et al. Engineering skeletal muscle tissues with advanced maturity improves synapse formation with human induced pluripotent stem cell-derived motor neurons. *APL Bioeng*. **5**, (2021).
44. Squire, J. M. Architecture and function in the muscle sarcomere. *Curr. Opin. Struct. Biol.* **7**, 247–257 (1997).
45. Zhao, H. et al. Compliant 3D frameworks instrumented with strain sensors for characterization of millimeter-scale engineered muscle tissues. *Proc. Natl. Acad. Sci. USA* **118**, e2100077118 (2021).
46. Morita, K., Morimoto, Y. & Takeuchi, S. Biohybrid tensegrity actuator driven by selective contractions of multiple skeletal muscle tissues. *Biofabrication* **15**, 045002 (2023).
47. Filippi, M. et al. Multicellular muscle-tendon bioprinting of mechanically optimized musculoskeletal bioactuators with enhanced force transmission. *Sci. Adv.* **11**, eadv2628 (2025).
48. Thandiackal, R. et al. Emergence of robust self-organized undulatory swimming based on local hydrodynamic force sensing. *Sci. Robot.* **6**, eabf6354 (2021).
49. Katzschmann, R. K., DelPreto, J., MacCurdy, R. & Rus, D. Exploration of underwater life with an acoustically controlled soft robotic fish. *Sci. Robot.* **3**, eaar3449 (2018).
50. Hartmann, F. et al. Highly agile flat swimming robot. *Sci. Robot.* **10**, eadr0721 (2025).
51. Li, G. et al. Underwater undulating propulsion biomimetic robots: A review. *Biomimetics* **8**, 318 (2023).
52. Farina, S. C. & Summers, A. P. Boxed up and ready to go. *Nature* **517**, 274–275 (2015).
53. Zajac, F. E. Muscle and tendon: properties, models, scaling, and application to biomechanics and motor control. *Crit. Rev. Biomed. Eng.* **17**, 359–411 (1989).
54. Lynch, N. et al. Enhancing and decoding the performance of muscle actuators with flexures. *Adv. Intell. Syst.* **6**, 2300834 (2024).
55. Backx, P., De Tombe, P., Van Deen, J., Mulder, B. & Ter Keurs, H. A model of propagating calcium-induced calcium release mediated by calcium diffusion. *J. Gen. Physiol.* **93**, 963–977 (1989).
56. Lichtwark, G. A. & Wilson, A. M. A modified Hill muscle model that predicts muscle power output and efficiency during sinusoidal length changes. *J. Exp. Biol.* **208**, 2831–2843 (2005).
57. Zuurbier, C. J., Everard, A. J., van der Wees, P. & Huijing, P. A. Length-force characteristics of the aponeurosis in the passive and active muscle condition and in the isolated condition. *J. Biomech.* **27**, 445–453 (1994).
58. Roberts, T. J. Contribution of elastic tissues to the mechanics and energetics of muscle function during movement. *J. Exp. Biol.* **219**, 266–275 (2016).
59. Lichtwark, G. A. & Wilson, A. M. Is Achilles tendon compliance optimised for maximum muscle efficiency during locomotion?. *J. Biomech.* **40**, 1768–1775 (2007).
60. Lichtwark, G. A. & Wilson, A. M. Optimal muscle fascicle length and tendon stiffness for maximising gastrocnemius efficiency during human walking and running. *J. Theor. Biol.* **252**, 662–673 (2008).
61. Nosaka, K., Aldayel, A., Jubeau, M. & Chen, T. C. Muscle damage induced by electrical stimulation. *Eur. J. Appl. Physiol.* **111**, 2427–2437 (2011).
62. Nakayama, K. H., Shayan, M. & Huang, N. F. Engineering biomimetic materials for skeletal muscle repair and regeneration. *Adv. Healthc. Mater.* **8**, 1801168 (2019).
63. Long, J. H. & Nipper, K. S. The importance of body stiffness in undulatory propulsion. *Am. Zool.* **36**, 678–694 (1996).
64. Quinn, D. & Lauder, G. Tunable stiffness in fish robotics: mechanisms and advantages. *Bioinspir. Biomim.* **17**, 011002 (2021).
65. Zhong, Q. et al. Tunable stiffness enables fast and efficient swimming in fish-like robots. *Sci. Robot.* **6**, eabe4088 (2021).
66. Bujard, T., Giorgio-Serchi, F. & Weymouth, G. D. A resonant squid-inspired robot unlocks biological propulsive efficiency. *Sci. Robot.* **6**, eabd2971 (2021).
67. Zimmerman, J. F. et al. Bioinspired design of a tissue-engineered ray with machine learning. *Sci. Robot.* **10**, eadr6472 (2025).
68. Rezakhaniha, R. et al. Experimental investigation of collagen waviness and orientation in the arterial adventitia using confocal laser scanning microscopy. *Biomech. Model. Mechanobiol.* **11**, 461–473 (2012).

Acknowledgements

Y.J.T. acknowledges the NUS start-up grant, the Ministry of Education, Singapore, under MOE AcRF Tier 1, and the Robotics Grand Challenge. We thank L. Zhu and Z. Qin for discussion regarding mathematical modeling.

Author contributions

P.C. and Y.J.T. conceived the idea and designed the experiments. P.C. carried out experiments, collected and analyzed the overall data. P.C. and X.W. contributed to the muscle contraction model. X.W. designed and fabricated the electrical stimulation and force measurement setup. J.Z. and P.C. drew the illustrations. Y.J.T. supervised the project. P.C. and X.W. cowrote the paper. All authors discussed the results and commented on the manuscript.

Competing interests

The authors declare no competing interests.

Additional information

Supplementary information The online version contains supplementary material available at https://doi.org/10.1038/s41467-026-70259-9.

Correspondence and requests for materials should be addressed to Yu Jun Tan.

Peer review information *Nature Communications* thanks Maira Cordelle and the other anonymous reviewer(s) for their contribution to the peer review of this work. A peer review file is available.